atmosphere

MDPI

Article

Ensemble Predictions of Rainfall-Induced Landslide Risk under Climate Change in China Integrating Antecedent Soil-Wetness Factors

Han Zong, Qiang Dai * and Jingxuan Zhu

Key Laboratory of VGE of Ministry of Education, Nanjing Normal University, Nanjing 210023, China; hanzong@njnu.edu.cn (H.Z.); jingxuanzhu@njnu.edu.cn (J.Z.)
* Correspondence: q.dai@njnu.edu.cn

Abstract: Global warming has increased the occurrence of extreme weather events, causing significant economic losses and casualties from rainfall-induced landslides. China, being highly prone to landslides, requires comprehensive predictions of future rainfall-induced landslide risks. By developing a landslide-prediction model integrated with the CMIP6 GCMs ensemble, we predict the spatiotemporal distribution of future rainfall-induced landslides in China, incorporating antecedent soil-wetness factors. In this study, antecedent soil wetness is represented by the antecedent effective rainfall index (ARI), which accounts for cumulative rainfall, evaporation, and runoff losses. Firstly, we calculated landslide susceptibility using seven geographic factors, such as slope and geology. Then, we constructed landslide threshold models with two antecedent soil-wetness indicators. Compared to the traditional recent cumulative rainfall thresholds, the landslide threshold model based on ARI demonstrated higher hit rates and lower false alarm rates. Ensemble predictions indicate that in the early 21st century, the risk of landslides decreases in the Qinghai–Tibet Plateau, Southwest, and Southeast regions but increases in other regions. Mid-century projections show a 10% to 40% increase in landslide risk across most regions. By the end of the century, the risk is expected to rise by more than 15% nationwide, displaying a spatial distribution pattern that intensifies from east to west.

Keywords: rainfall-induced landslides; ensemble prediction; antecedent soil-wetness factors; climate change

check for updates

Citation: Zong, H.; Dai, Q.; Zhu, J. Ensemble Predictions of Rainfall-Induced Landslide Risk under Climate Change in China Integrating Antecedent Soil-Wetness Factors. *Atmosphere* **2024**, *15*, 1013. https://doi.org/10.3390/atmos15081013

Academic Editor: Stefano Federico

Received: 18 July 2024
Revised: 9 August 2024
Accepted: 19 August 2024
Published: 21 August 2024

1. Introduction

In recent years, global warming has become a significant global concern. Rising temperatures have increased the frequency and intensity of extreme events, leading to various natural disasters and posing significant risks to ecosystems and human societies. Among these, rainfall-induced landslides are particularly sensitive to climate change. China is heavily impacted by landslides, with approximately 90% triggered by intense or prolonged rainfall [1]. According to the "National Geological Disaster Bulletin", from 2007 to 2020, China experienced 200,000 geological disasters, 66.31% of which were landslides, resulting in 8170 deaths or missing persons, 3850 injuries, and direct economic losses of 60.51 billion yuan [2]. To mitigate the impact of rainfall-induced landslides, it is essential to predict and assess landslide risks under future climate change conditions, providing a scientific basis for disaster prevention and mitigation strategies.

The causes of landslides are complex, involving both internal environmental conditions and external triggering factors [3]. Internal conditions include the slope's lithology, topography, hydrology, and geological characteristics. External factors, such as rainfall and earthquakes, provide the dynamic conditions that trigger landslides. Most landslides result from the interaction between these internal conditions and external triggers [4].

Landslide-susceptibility assessment methods are used to evaluate the influence of static factors on landslide occurrence and predict the possibility of landslides in a specific area, often referred to as landslide susceptibility analysis [5–7]. These methods typically use geographic information systems (GIS) to collect data on static factors like geology, topography, hydrology, soil, and vegetation. Statistical analysis is then employed to develop landslide susceptibility models, which are essential tools for regional landslide spatial prediction [8]. In the tropical environment of Malaysia, Himan Shahabi and Mazlan Hashim used GIS-based statistical models and remote sensing data to achieve landslide-susceptibility calculations with an accuracy of up to 96% [9]. Amina Abdi et al. employed GIS-based fuzzy logic and the analytic hierarchy process to map landslide susceptibility. They found that the fuzzy logic method was more effective in assessing landslide susceptibility, demonstrating higher consistency and accuracy [10].

For the external triggering factors, earthquakes and rainfall are different in their regime to trigger a landslide. In this study, we focus on rainfall-triggered landslides. Most research focuses on the relationship between landslides and rainfall, and the methods used are mainly divided into theoretical and statistical analyses [11–14]. Theoretical analysis investigates the mechanisms of rainfall-induced landslides by developing physical models [15]. However, due to the complexity of physical processes and specific characteristics, this approach is more suitable for studying region-limited slopes and is ineffective for large-scale landslide prediction.

Statistical analysis methods rely on extensive historical landslide data and associated rainfall information. By establishing statistical relationships between landslides and rainfall, researchers can determine rainfall threshold values that trigger landslides. This approach is the most commonly used for landslide prediction. Rainfall thresholds, the critical values at which rainfall induces slope instability, vary based on the rainfall characterization variables used. When only cumulative rainfall is considered, the threshold is a specific value, such as the 1-day or 3-day cumulative rainfall threshold [16]. When two rainfall variables are considered together, the threshold typically takes the form of a power function curve [17]. Statistical analysis methods have been widely applied in practice and play a significant role in landslide prediction and early warning. Statistics indicate that approximately three-quarters of the world's landslide-prediction and early warning systems are based on empirical rainfall threshold frameworks [18].

Apart from the rainfall that triggers a landslide, the soil water content affected by antecedent rainfall has been proved to be important for the occurrence of a landslide as well [19–21]. Antecedent rainfall raises the water content in slope materials, increasing pore water pressure, reducing stability, and triggering landslides. Some research used antecedent soil moisture for the prediction of landslides; however, the acquisition of antecedent soil moisture is challenging and exhibits significant spatial heterogeneity, necessitating the use of more complex models for accurate prediction [22]. On the other hand, antecedent rainfall is easily obtainable and can be monitored in real time using weather stations and satellite data. Thus, considering antecedent rainfall can effectively account for slope stability influenced by previous soil-moisture conditions [23].

Climate change-induced increases in surface temperatures and alterations in precipitation patterns have led to more frequent extreme rainfall events in many regions worldwide [24]. In China, He et al. first utilized a landslide statistical forecasting model and the regional climate model RegCM4.0 to project a significant increase in landslides during the 21st century under the high emission scenario RCP8.5 [25]. Similarly, Ge et al. employed global climate model precipitation data and statistical models to forecast that, under the RCP8.5 scenario in 2050, the landslide risk in China will generally rise [26]. However, these studies only considered the precipitation but ignored the antecedent soil wetness, which inevitably influences the occurrence of rainfall-induced landslides and other geological disasters [27].

In summary, this study develops two methods based on cumulative rainfall and the antecedent soil-wetness index, respectively, to assess the landslide risk in China under climate change. These methods are integrated with topography, geomorphology, and rock-soil characteristics to construct a landslide threshold model. Using multiple CMIP6

GCM ensembles, the models simulate rainfall-induced landslides under climate change scenarios. The aim is to project changes in the distribution of rainfall-induced landslides in China under future climate scenarios, identify high-risk areas, and provide a scientific basis for disaster prevention and mitigation.

2. Study Area and Data

The study area of this research is China, which is situated in the eastern part of the Eurasian continent, on the western coast of the Pacific Ocean. Its geographical coordinates extend from 73°40′ E to 135°2′30″ E and from 3°52′ N to 53°55′ N, encompassing a land area over 9.6 million km^2. Due to the diverse climatic conditions, land features, and other geographical environments across its vast territory, the occurrence of landslides varies significantly from region to region.

To construct the landslide-prediction model, this study utilized the following data:

Rainfall. This study used the CHIRPS (Climate Hazards group InfraRed Precipitation with Station data) satellite rainfall product, developed by the U.S. Geological Survey and the Climate Hazards Group at the University of California, Santa Barbara. CHIRPS offers multiple temporal scales (daily to monthly), spatial resolutions (0.05° to 0.25°), near-global coverage (50° S to 50° N), and long-term records (from 1981 to the present). The dataset used in this study spans from 1 January 1981 to 31 December 2020, with a spatial resolution of 0.05° × 0.05°.

Temperature. This study used the CHIRTS (Climate Hazards Center InfraRed Temperature with Stations data) daily temperature dataset, developed by the Climate Hazards Center at the University of California, Santa Barbara. This product provides daily maximum and minimum temperatures from 1983 to 2016, covering latitudes from 60° S to 70° N, with resolutions of 0.25° × 0.25° and 0.05° × 0.05°. We used the CHIRTS dataset with the 0.05° × 0.05° resolution to obtain daily average temperatures. To address data gaps in CHIRTS (1981–1982 and 2017–2020), we supplemented it with the CN05.1 daily observational dataset (0.25° × 0.25°) published by the National Climate Center of the China Meteorological Administration [28], applying bilinear interpolation to align the resolution.

Climate datasets. This study also incorporates multi-model climate datasets from the Coupled Model Intercomparison Project Phase 6 (CMIP6). To ensure consistency, we selected 15 climate models from the same experiment run (rli1p1f1) (Table 1). Each model provides daily precipitation and temperature data for both the reference period (1981–2014) and the projection period (2015–2100). The climate change scenarios used are SSP1-2.6, SSP2-4.5, and SSP5-8.5. The reference period is set from 1981 to 2014, and the future period is set from 2015 to 2100; this is further divided into near-term (2015–2040), mid-term (2041–2070), and long-term (2071–2100).

Table 1. Basic information of CMIP6.

Paradigm	Country	Institution (Abbr.)	Resolution (Grid Points in Latitude × Longitude Directions)
ACCESS-CM2	Australia	CSIRO-ARCCSS	192 × 144
ACCESS-ESM1-5	Australia	CSIRO	192 × 144
CESM2-WACCM	Australia	CMCC	288 × 192
EC-Earth3-Veg	European Union	EC-Earth-Consortium	512 × 256
FGOALS-g3	China	CasESM	180 × 80
GFDL-CM4	USA	NOAA-GFDL	288 × 180
GFDL-ESM4	USA	NOAA-GFDL	288 × 180
INM-CM4-8	Russia	INM	180 × 120
INM-CM5-0	Russia	INM	180 × 120
IPSL-CM6A-LR	France	IPSL	144 × 143
MIROC6	Japan	MIROC	256 × 128
MPI-ESM1-2-LR	Germany	MPI-M	192 × 96
MRI-ESM2-0	Japan	MPI	320 × 160
NorESM2-LM	Norway	NCC	144 × 96
NorESM2-MM	Norway	NCC	288 × 192

Although CMIP6 has improved in its model accuracy and resolution, significant discrepancies still exist between GCM-simulated climate changes and the actual climate system due to its complexity. These discrepancies make it challenging to use GCM simulations directly for future climate change predictions. To achieve more accurate future rainfall-induced landslide simulations that reflect the real conditions of the study area, it is necessary to ensure that GCM simulation data used as driving conditions for the landslide-prediction model align with actual climate conditions. Therefore, this study employs the grid as the basic unit and uses Quantile Delta Mapping (QDM) and Multivariate Bias Correction (MBC) methods to correct biases in the GCMs [29,30]. Additionally, to address the resolution differences between GCMs-simulated rainfall and observed rainfall (CHIRPS) and to ensure consistency across models, the Spatial Disaggregation (SD) method is applied to downscale the bias-corrected models, standardizing the resolution to $0.05° \times 0.05°$ [31,32].

Landslides dataset. We used an observation dataset of landslide to validate the landslide-prediction model. The records are from the Global Landslide Catalog (GLC), with examples of landslide information provided in Table 2. Since this study focuses on rainfall-induced landslides, the GLC database was further filtered by the triggering factor. Given the sparse landslide records before 2005, we selected events that occurred in China post-2006 and were triggered by rainfall. This process resulted in a final selection of 482 rainfall-induced landslide records.

Table 2. Example of selected GLC data.

Date and Time	Triggering Factor	Scale	Casualties	Country	Longitude	Latitude
1 August 2008 12:00:00 AM	rain	large	11	China	107.45	32.56
19 February 2013 11:00:00 AM	mining	medium	5	China	107.93	26.66
21 January 2013 02:00:00 PM	earthquake	medium	0	New Zealand	170.18	−43.56
15 March 2015 11:00:00 PM	snowfall/ snowmelt	medium	0	India	75.30	33.08
1 May 2015 12:00:00 AM	earthquake	small	16	China	85.96	9.98

3. Methodology

This study employs the LHASA (Landslide Hazard Assessment for Situational Awareness) model for assessing landslide risk. Developed by the NASA Goddard Space Flight Center, this model aims to identify potential landslides and provide near-real-time warning signals [33]. The model includes two components: static variables contributing to slope instability (landslide sensitivity maps) and a threshold model for landslide prediction.

The decision-making process of the LHASA model is shown in Figure 1. First, hydrometeorological characteristics, such as cumulative rainfall and the antecedent effective rainfall index, are obtained for each grid cell. Using the relationship between these factors and historical landslides, a landslide threshold model is constructed to determine if an extreme rainfall warning should be issued. If no extreme rainfall warning is issued, landslides are unlikely to occur in the area. If an extreme rainfall warning is issued, the sensitivity map is then considered. Areas with low sensitivity have a low probability of landslides and do not receive a risk warning. Areas with medium sensitivity receive a moderate-risk warning, and areas with high sensitivity receive a high-risk warning.

3.1. Bias Correction of Climate Models

Due to the inherent complexity of the climate system, GCMs often exhibit significant biases when simulating climate changes, making direct use of these models for future climate predictions challenging. Therefore, it is essential to correct the GCM data to match the actual climate conditions of the region before they can be used as inputs for the landslide-prediction models. Two bias-correction methods are employed: Quantile Delta Mapping (QDM), proposed by Cannon et al. (2015) [30], and Multivariate Bias Correction (MBC), which uses N-dimensional Probability Density Function Transform (N-pdft), as described by Cannon (2018) [29]. This study uses 1981 to 2010 as the reference period and 2011 to 2014 as the validation period, with grids serving as the basic unit for bias correction.

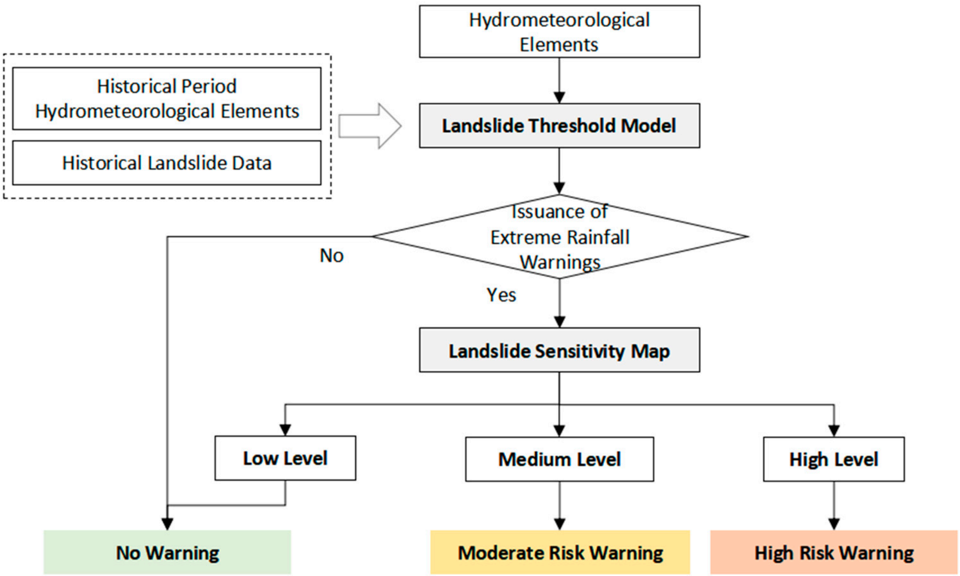

Figure 1. The decision-making process of the LHASA model.

(1) Quantile Delta Mapping (QDM)

QDM operates on the assumption that the biases in climate models are consistent over time, implying that the biases observed in the historical period will persist into the future. First, simulated precipitation values are adjusted using the inverse of the observed precipitation-distribution function to correct systematic biases. Next, the relative changes in quantiles between the historical and future periods are calculated. Finally, these factors are combined to yield bias-corrected precipitation values. Thus, QDM effectively corrects the model's systematic biases while preserving the relative changes projected by the model. The specific calculation formula is as follows:

$$p_{0:m,n:f} = F_{0,h}^{-1}\left(F_{m,f}\left(p_{m,f}\right)\right) \tag{1}$$

$$\Delta m = \frac{F_{mf}^{-1}\left(F_{m,f}\left(p_{m,f}\right)\right)}{F_{m,h}^{-1}\left(F_{m,f}\left(p_{m,f}\right)\right)} = \frac{p_{m,f}}{F_{m,h}^{-1}\left(F_{m,f}\left(p_{m,f}\right)\right)} \tag{2}$$

$$\hat{p}_{m,f} = p_{o:m,h:f} \cdot \Delta_m \tag{3}$$

In this formula, $p_{o,h}$ represents the observed precipitation during the historical period, and $p_{m,f}$ denotes the simulated precipitation for the future period. The terms $F_{m,f}$ and $F_{m,h}$ refer to the cumulative distribution functions of the model for the historical and future periods, respectively. $p_{o:m,h:f}$ is the detrended simulated precipitation for the future period, Δ_m indicates the model's predicted trend value, and $\hat{p}_{m,f}$ represents the bias-corrected simulated precipitation for the future period.

(2) Multivariate Bias Correction Method (MBCn)

The MBCn method extends QDM to a multivariate framework by integrating QDM with the image-processing technique known as N-pdft. In the context of climate model bias correction, Cannon applied orthogonal transformations to create linear combinations of original variables, facilitating univariate quantile mapping bias correction for multivariate distributions. The algorithm consists of three steps:

First, an N × N uniformly distributed random orthogonal matrix $R[j]$ is constructed, and orthogonal transformations are applied to both the source and target data.

$$\tilde{X}_S^{[j]} = X_S^{[j]} R^{[j]} \tag{4}$$

$$\tilde{X}_P^{[j]} = X_P^{[j]} R^{[j]} \tag{5}$$

$$\tilde{X}_T^{[j]} = X_T^{[j]} R^{[j]} \tag{6}$$

In the formula, X_S denotes the simulated data for the historical period, X_P denotes the simulated data for the future period, X_T denotes the observed data for the historical period, and j denotes the iteration count.

Second, the orthogonally transformed data are input into Formulas (4)–(6) to adjust their marginal distributions using the QDM method. Finally, the results are inversely transformed. These three steps are repeated iteratively until the multivariate distribution aligns with the target distribution. In this study, we chose to perform 30 iterations [29].

$$X_S^{[j+1]} = \hat{X}_S^{[j]} R^{[j]^{-1}} \tag{7}$$

$$X_P^{[j+1]} = \hat{X}_P^{[j]} R^{[j]^{-1}} \tag{8}$$

$$X_T^{[j+1]} = X_T^{[j]} \tag{9}$$

3.2. Landslide-Sensitivity Calculation

This study integrates the landslide-sensitivity calculation methods of Stanley and Kirschbaum [34] by using a fuzzy overlay model to combine seven environmental factors (slope, geological lithology, distance to fault zones, roads, water systems, newly developed urban areas, and forest loss) into a 1-km resolution sensitivity map of China.

Firstly, the nonlinear relationship between environmental factors and landslide sensitivity is modeled using fuzzy membership functions, which convert the characteristic values of these factors into membership degrees ranging from 0 to 1, where higher values indicate greater sensitivity. Then, the "fuzzy gamma" operator is employed to combine these membership degrees, producing the initial sensitivity output set.

To facilitate understanding and further use, the sensitivity values are classified into five categories: very low, low, medium, high, and very high. The number of grid cells in each category increases progressively. For instance, the "very low" category contains twice as many grid cells as the "low" category, and the "low" category contains twice as many as the "medium" category. Ultimately, the "very low" and "low" categories are combined into low sensitivity, the "medium" and "high" categories into medium sensitivity, and the "very high" category remains as high sensitivity. Low sensitivity indicates a lower likelihood of landslides in the area, while high sensitivity indicates a higher likelihood of landslides [34].

3.3. Construction of the Landslide Threshold Model

This study develops a univariate threshold model, where a single variable's critical value serves as the landslide-triggering threshold. First, historical rainfall data is collected to create a continuous dataset. Each grid cell is assigned an extreme value, defined as the 95th percentile of historical rainfall, as the landslide threshold. Comparing target rainfall to this threshold allows for determining the likelihood of a landslide event in the area.

In constructing the univariate rainfall threshold model, cumulative rainfall and antecedent effective rainfall are used as rainfall characterization variables, denoted as MODEL 1 and MODEL 2, respectively. This approach is chosen because relying solely on daily rainfall is not sufficient to judge extreme rainfall events. Continuous rainfall over several days can increase soil moisture, potentially triggering landslides even if the daily rainfall is low. Therefore, assessing landslide risk based only on daily rainfall is inadequate.

Studies by Mirus et al. have shown that incorporating 3-day antecedent rainfall improves the performance of landslide-prediction models. Additionally, using a 3-day period to distinguish between antecedent and recent rainfall is common in other studies [35]. To better evaluate the impact of rainfall on landslides, the rainfall from the 3 days preceding an event is used as a recent rainfall indicator, named as 3-day cumulative rainfall.

As soil wetness is difficult to measure in high spatial-temporal resolution and it is highly related to rainfall, in this study the antecedent effective rainfall index is utilized to represent the soil-wetness condition, based on prior daily rainfall data. It should be noted that the antecedent effective rainfall index functions as a soil moisture index, enabling the estimation of the relative wetness condition of the soil [36]. The antecedent effective rainfall index accounts for losses due to processes like evaporation and runoff by using a decay coefficient. After these losses are deducted, the antecedent rainfall is accumulated. The calculation equation is as follows:

$$ARI = \frac{\sum_0^t p_t w_t}{\sum_0^t w_t} \quad (10)$$

$$w_t = (t+1)^{-w} \quad (11)$$

In the equation, t represents the number of prior days, p_t denotes the rainfall on the t-th day before, and w_t is the decay coefficient, a weight assigned to the rainfall on the t-th day before.

This formula shows that the antecedent effective rainfall index is determined by the combination of the number of days and the decay coefficient. Different choices of t significantly impact the model. To find the optimal number of days, we compare 3-day and 7-day antecedent rainfall amounts, with the decay coefficient w ranging from 1 to 3. When w = 1, the ARI equals the cumulative antecedent rainfall without any decay. Higher values of w indicate greater losses of antecedent rainfall due to evaporation and runoff.

To determine the optimal parameters, this study used CHIRPS rainfall data from 1981 to 2018 for calibration and validation. By combining different values of t and w, we generated the antecedent effective rainfall index (ARI) series for 1981–2018. Since most landslide records are from 2008–2018, we used the 95th percentile of ARI from 1981–2007 as the historical threshold. Landslide data from the GLC database and 5000 additional non-landslide time-location points were selected, with 80% used for calibration and 20% for validation (validation results in Section 4.2). We calculated the ARI for each event under different parameters and used its exceedance of the historical threshold to predict landslides. The optimal t and w were determined by the Euclidean distance with the detailed calculation described in Section 3.3. The parameter calibration results are shown in Figure 2. The Euclidean distance decreases sharply with increasing w, with the 3-day ARI significantly larger than the 7-day ARI. Beyond w = 2, the decrease stabilizes, and the 3-day ARI's Euclidean distance becomes smaller than the 7-day ARI. At w = 2.3, the 3-day ARI's Euclidean distance is minimized to 0.3583, making 3 days and 2.3 the optimal combination.

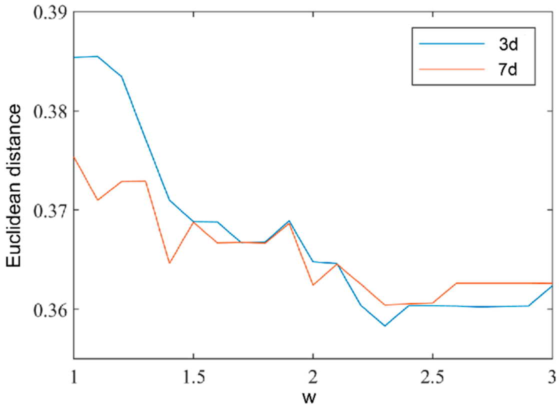

Figure 2. Calibration of parameters with Euclidean distances for different w and t values.

3.4. Landslide-Prediction Model Evaluation

Landslide-detection results can be classified into four categories: True Positive (TP), False Positive (FP), True Negative (TN), and False Negative (FN). True Positives are actual landslides correctly identified by the model. False Positives are non-landslides incorrectly identified as landslides by the model. True Negatives are non-landslides correctly identified by the model. False Negatives are actual landslides incorrectly identified as non-landslides by the model. Based on these categories, we can calculate evaluation metrics such as hit rate, false alarm rate, and Euclidean distance. The specific equations for these calculations are shown below.

(1) Hit Rate

The hit rate, also known as the True Positive Rate (TPR), is the proportion of correctly detected landslide events among all landslide events. The optimal value is 1. The calculation equation is as follows:

$$TPR = \frac{TP}{TP + FN} \tag{12}$$

(2) False Alarm Rate

The false alarm rate, or False Positive Rate (FPR), is the proportion of non-landslide events incorrectly reported as landslides among all non-landslide events. The optimal value is 0. The calculation equation is as follows:

$$FPR = \frac{FP}{FP + TN} \tag{13}$$

(3) Euclidean Distance

The optimal classification result occurs when the hit rate is 1 and the false alarm rate is 0. To better evaluate the performance of the landslide-prediction model, we use the Euclidean distance, which considers both the hit rate and the false alarm rate. The model performance is assessed by calculating the Euclidean distance (d) between the prediction results and the optimal value. A smaller distance indicates better model performance. The calculation equation is as follows:

$$d = \sqrt{FPR^2 + (TPR - 1)^2} \tag{14}$$

(4) Spatial Buffer and Time Window

Before conducting landslide-risk estimation, it is essential to evaluate the model performance using landslide records. Historical landslide records may have inaccuracies, such as delayed recording times and location displacements. To address these, spatial buffers and time windows are established for model validation. Spatial buffers correct location errors, while time windows address timing inaccuracies. We use a spatial buffer radius of one grid cell. Time windows of 1, 3, and 7 days are selected. A 1-day window assumes no timing error. A 3-day window accounts for a possible 1-day deviation before or after the recorded time. A 7-day window allows for errors ranging from 5 days before to 1 day after the recorded time. The range of 5 days before and 1 day after is chosen because field records typically note the discovery day or a few days before, rather than after [33].

4. Results

4.1. Assessment of Landslide Sensitivity

This study employs a heuristic approach, considering various factors contributing to landslides, to calculate landslide sensitivity. The sensitivity values are categorized into five levels: very low, low, medium, high, and very high, and the map of rainfall-induced landslide sensitivity levels in China is shown in Figure 3. The results indicate that areas with medium to high sensitivity are primarily located in regions with rugged terrain and significant tectonic activity, such as the Hengduan Mountains, Yunnan–Guizhou Plateau, and southeastern hilly areas. In contrast, the Inner Mongolia Plateau, North China Plain, and Northeast Plain, characterized by flat terrain, have lower sensitivity levels and a lower likelihood of landslides. This study deems low-sensitivity areas as unlikely to experience landslides. Therefore, subsequent research will focus on regions with medium and high sensitivity.

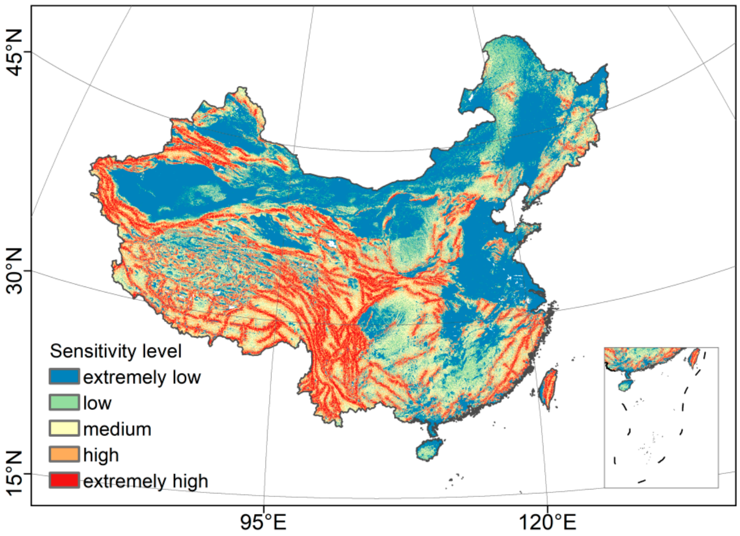

Figure 3. Map of rainfall-induced landslide sensitivity levels in China.

To verify the feasibility of this landslide-sensitivity calculation method in China, this study counted the number of landslides in different sensitivity levels (Table 3). The accuracy of the landslide-sensitivity results increases if more landslides fall into the medium- and high-sensitivity categories. Among the 404 recorded rainfall-induced landslides, 14.36% occurred in low-sensitivity areas, 32.43% in medium-sensitivity areas, and 53.22% in high-sensitivity areas. Low-sensitivity areas, which are mostly flat regions, are generally not prone to landslides. However, extreme rainfall or earthquake events could trigger landslides in these areas, although such occurrences are relatively rare. Consequently, this study does not consider low-sensitivity areas. Validation results indicate that the sensitivity map produced by this method effectively captures most landslide-prone areas and can be used for subsequent rainfall-induced landslide-prediction models.

Table 3. Percentage of landslide points (%) in different sensitivity levels.

Sensitivity Level	**Low**		**Medium**		**High**
	1	**2**	**3**	**4**	**5**
	5.04	9.32	15.64	16.79	53.22
Total	14.36		32.43		53.22

4.2. Validation of the Landslide Threshold Models

Landslide threshold models were developed using the calculated 3-day cumulative rainfall (MODEL 1) and the antecedent effective rainfall index (MODEL 2). Historical thresholds for these variables were established. According to the LHASA model decision process, an event is evaluated based on two conditions: (1) it occurs in a medium- to high-sensitivity area, and (2) the 3-day cumulative rainfall or ARI exceeds the historical threshold. If both conditions are met, a moderate- or high-risk warning is triggered. Table 4 presents the number of successful landslide warnings by MODEL 1 and MODEL 2, with and without spatial buffers and time windows. Without a spatial buffer and with a 1-day time window, warnings are issued exactly on the landslide's recorded date, with hit rates below 40%. MODEL 1 shows a higher hit rate than MODEL 2 in this scenario. However, with 3-day and 7-day time windows, MODEL 2 achieves a higher hit rate. Introducing a spatial buffer increases the hit rate for each time window by 10% to 20%. Regarding the false alarm rate, MODEL 2 outperforms MODEL 1.

Table 4. The validation accuracy (%) of MODEL 1 and MODEL 2.

			TPR			**FPR**
			1-Day	**3-Day**	**7-Day**	
MODEL 1	No Buffer	Medium Sensitivity	27.80	37.76	43.78	4.88
		High Sensitivity	40.00	52.55	58.43	6.63
	With Buffer	Medium Sensitivity	46.68	59.34	71.37	--
		High Sensitivity	54.90	69.02	80.78	--
MODEL 2	No Buffer	Medium Sensitivity	26.76	42.95	55.60	3.90
		High Sensitivity	37.65	58.82	73.73	5.47
	With Buffer	Medium Sensitivity	38.59	57.68	71.58	--
		High Sensitivity	44.71	67.84	80.00	--

4.3. Threshold Calculation for Prediction Models

From the validation, it is evident that the rainfall threshold model performs well in China, successfully providing early warnings for most landslides. To predict landslide risk in China under different GCMs, we calculated rainfall sequences for each GCM during the historical period (1981–2014), using the 95th percentile as the rainfall threshold. As shown in Figure 4, the threshold differences among the various GCMs are minimal. This is mainly contributed to bias correction and downscaling of the rainfall data for each model with observed data, resulting in similar temporal and spatial decay patterns. Additionally, over 30 years of rainfall data reflects regional climate stability, reducing randomness from interannual fluctuations, thereby making the rainfall thresholds of different models quite similar.

The thresholds for two models are shown in Figure 5. The Southeastern region of China exhibits higher thresholds, while the Northwestern inland areas have lower thresholds, decreasing from southeast to northwest. This pattern aligns with the distribution characteristics of China’s climate, where the Southeastern monsoon region receives more rainfall and the Northwestern inland region receives less.

4.4. Future Landslide Risk Prediction and Comparison

Based on the two landslide threshold models and the bias-corrected and downscaled CMIP6 GCMs data, this section predicts and evaluates the spatiotemporal characteristics of rainfall-induced landslide risk in China under 180 combinations of 15 GCMs, two landslide threshold models, three SSP scenarios, and two bias-correction methods. To quantify the relative change in future rainfall-induced landslide risk compared to the current state, the period from 1981 to 2014 is used as the climate reference period, and the relative change in landslide risk under future climate scenarios is calculated. The time periods covered are 2015–2040, 2041–2070, and 2071–2100, representing the early, middle, and late 21st century, respectively.

4.4.1. Spatiotemporal Changes in Landslide Risk Under Different Bias-Correction Methods

The landslide-risk predictions using the QDM and MBCn bias-correction algorithms were averaged to determine the spatiotemporal changes in landslide risk under different correction methods (Figure 6). Comparing the results, it is evident that the QDM algorithm predicts a higher increase in future landslide risk in China than the MBCn algorithm. In the early 21st century, only a small area shows a decreasing trend under the QDM algorithm, while over half of the regions show a decreasing trend under the MBCn algorithm, with the most significant decrease in the Qinghai–Tibet Plateau. Over time, landslide risk in the Eastern region increases significantly under both algorithms. However, in areas bordering the Qinghai–Tibet Plateau and the Northwest, the increase under the QDM algorithm exceeds 80%, while under the MBCn algorithm it is about 20% to 60%. Additionally, in the

Eastern Qinghai–Tibet Plateau, the decrease in landslide risk and the extent of this decrease are much greater under the MBCn algorithm than under the QDM algorithm. The results of the two bias-correction algorithms do not show significant differences; therefore, the subsequent analysis in this paper is based on the average of both algorithms.

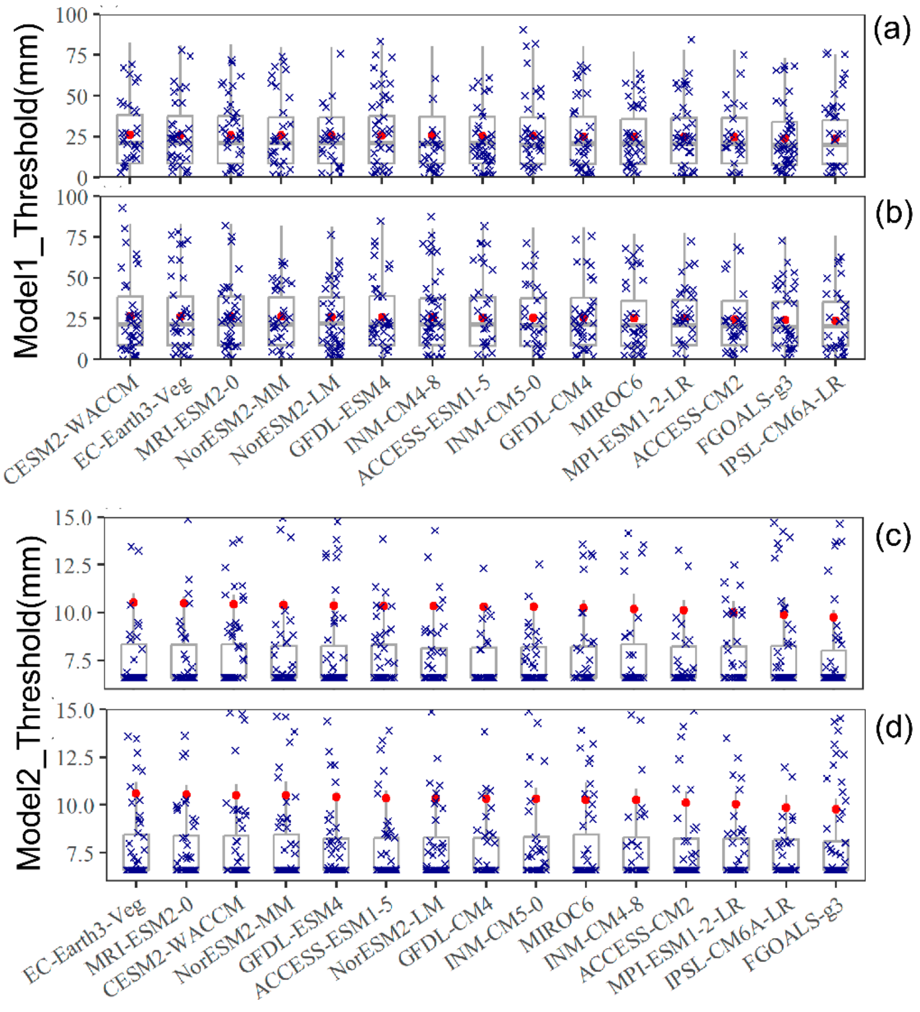

Figure 4. Thresholds of MODEL 1 and MODEL 2 under different climate models (red dots represent average values), (**a**) The thresholds of MODEL 1 under the QDM correction algorithm; (**b**) The thresholds of MODEL 1 under the MBCn correction algorithm; (**c**) The thresholds of MODEL 2 under the QDM correction algorithm; (**d**) The thresholds of MODEL 2 under the MBCn correction algorithm.

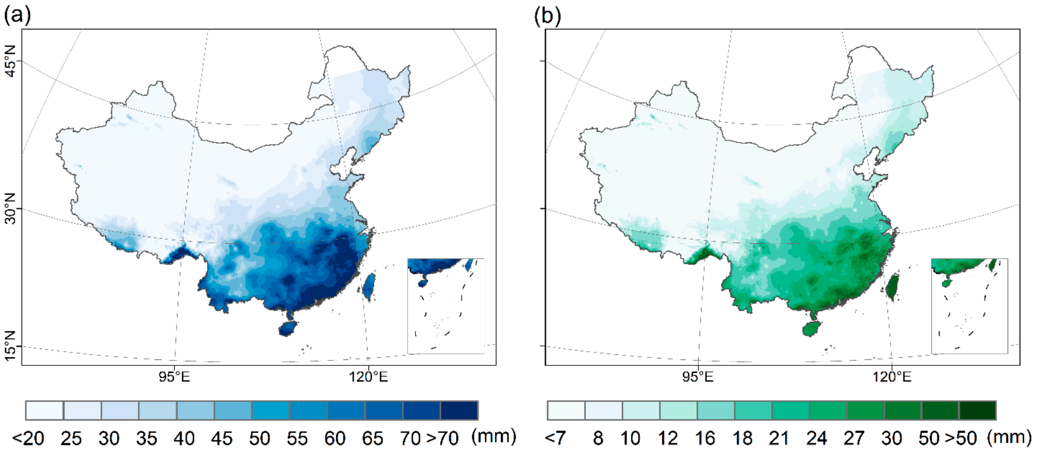

Figure 5. Spatial distribution of MODEL 1 and MODEL 2 thresholds, (**a**) MODEL 1; (**b**) MODEL 2.

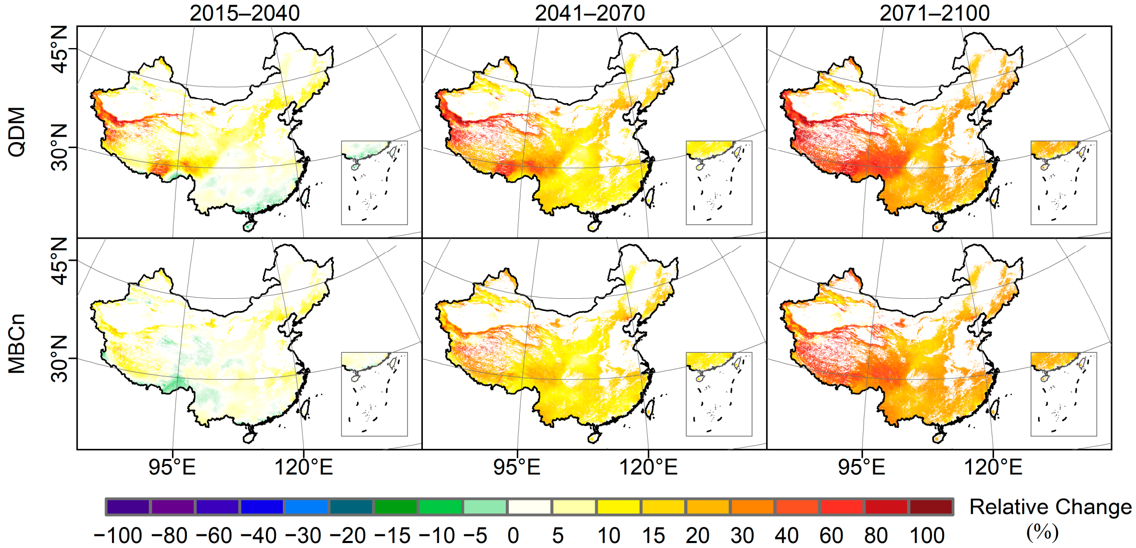

Figure 6. Spatial distribution of relative changes in rainfall-induced landslides in China under different bias-correction methods.

4.4.2. Spatiotemporal Changes in Landslide Risk Under Different SSP Scenarios

To investigate the spatiotemporal changes in landslide risk under different SSP scenarios, the ensemble means of landslide-risk predictions for SSP1-2.6, SSP2-4.5, and SSP5-8.5 scenarios are presented in Figure 7. In the early 21st century, all three scenarios indicate an increasing landslide risk in the Northern region and a decreasing risk in the Southern region, with similar magnitudes of change. By the late 21st century, the differences in magnitude become more pronounced. Under the SSP1-2.6 and SSP2-4.5 scenarios, the Eastern region shows an increase of about 15–20%, while under the SSP5-8.5 scenario, the increase is about 20–30%. In the Qinghai–Tibet Plateau, where the risk is rising, the growth rate under SSP5-8.5 is significantly higher than under SSP2-4.5, which is in turn higher than under SSP1-2.6.

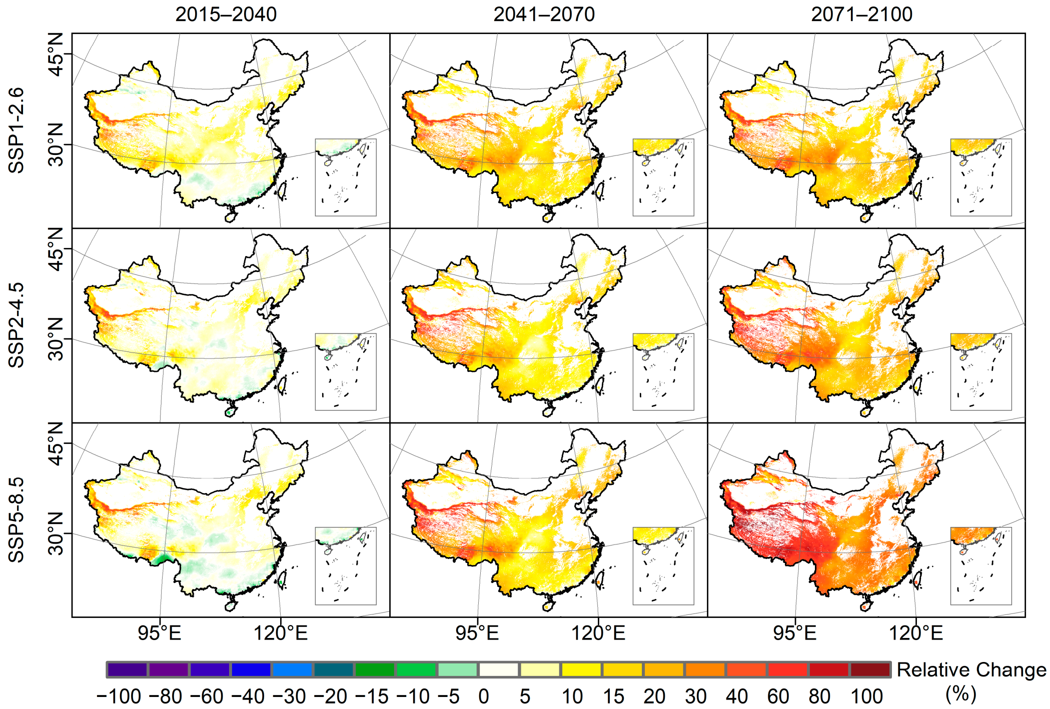

Figure 7. Spatial distribution of relative changes in rainfall-induced landslides in China under different SSP scenarios.

4.4.3. Spatiotemporal Changes in Landslide Risk Under Different GCMs

Here, we present an example of the ensemble mean of landslide risk prediction results for 2041–2070 under the SSP2-4.5 scenario in Figure 8. In the mid-21st century, the predicted trends, extents, and degrees of landslide risk vary across GCMs. Over half of the GCMs predict an increase in landslide risk in the southwest by 5% to 40%, while others foresee a decrease of 5% to 15% in this area. Several GCMs predict a decrease in landslide risk by less than 10% in the southern part of the Southeast region and an increase of about 5% in the northern part, while others predict a general increase in the Southeast by 5% to 20%. Most GCMs forecast an increase in landslide risk in the Northeast and Northern regions by 5% to 30%. NorESM2-MM predicts the largest area of decreasing trend nationwide, while ACCESS-ESM1-5 and GFDL-CM4 predict the largest areas of increasing trend.

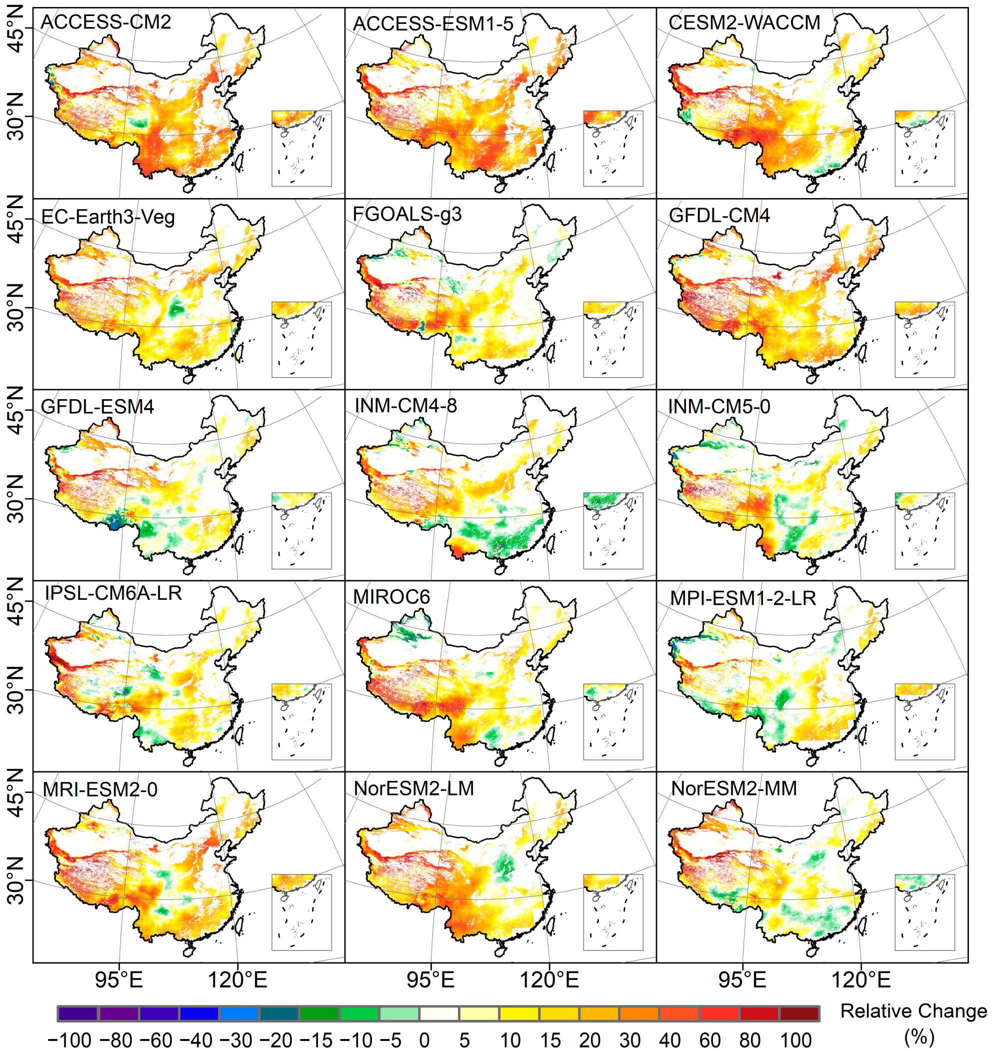

Figure 8. Spatial distribution of relative changes in rainfall-induced landslides in China from 2041 to 2070 under different climate models in the SSP2-4.5 scenario.

Figure 9 illustrates the relative changes in landslide risk predicted by different climate models under various Shared Socioeconomic Pathways (SSPs). Each model corresponds to specific SSP scenarios (SSP1-2.6, SSP2-4.5, SSP5-8.5). The data presented have been averaged across landslide threshold models and bias-correction methods. It is evident that most models forecast an increase in future landslide risk, with significant variability observed in models like CESM2-WACCM and INM-CM4-8. Overall, while the extent of landslide risk varies by model and SSP scenario, a general trend shows that the predicted increase in landslide risk is more pronounced under higher emission scenarios, such as SSP5-8.5.

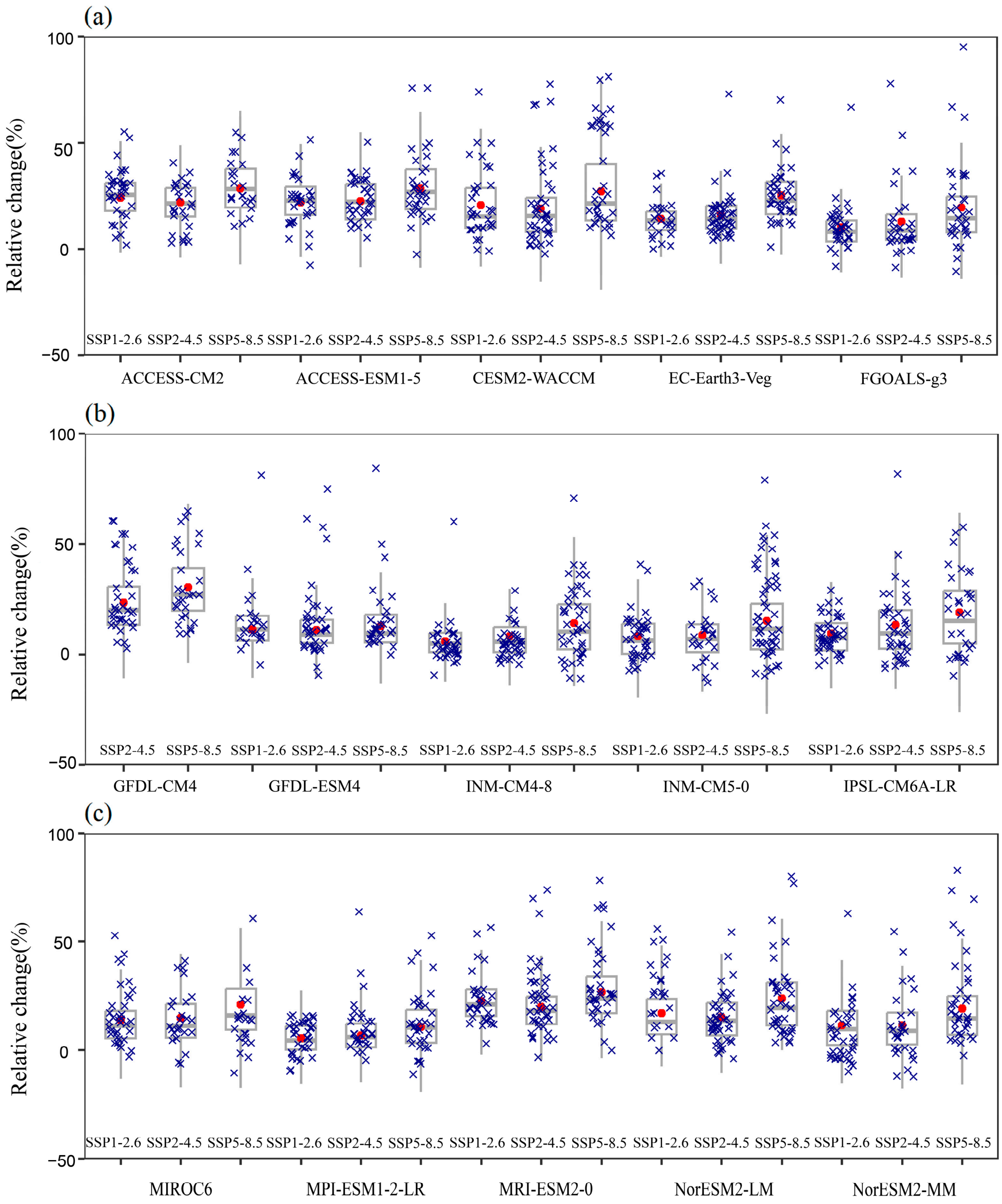

Figure 9. Relative changes in landslide risk under different SSPs across various climate models (red dots represent average values), (**a**) GCMs include ACCESS-CM2, ACCESS-ESM1-5, CESM2-WACCM, EC-Earth3-Veg, and FGOALS-g3; (**b**) GCMs include GFDL-CM4, GFDL-ESM4, INM-CM4-8, INM-CM5-0, and IPSL-CM6A-LR; (**c**) GCMs include MIROC6, MPI-ESM1-2-LR, MRI-ESM2-0, NorESM2-LM, and NorESM2-MM.

4.4.4. Spatiotemporal Changes in Landslide Risk under Different Threshold Models

We averaged the modeling results across SSPs, 15 GCMs, and two bias-correction methods (MBCn and QDM) separately for MODEL 1 and MODEL 2 to present a comprehensive and robust analysis. Then, the averaged results of MODEL 1 and MODEL 2 are compared to illustrate the differences between the two landslide threshold models, as shown in Figure 10. In the early 21st century, overall changes for both models range from −5% to 40%. The areas of decrease are concentrated in the South and the Eastern Qinghai–Tibet Plateau, while the regions with the highest increase are in the border areas of the Qinghai–Tibet Plateau and the Northwest. In the mid to late 21st century, landslide risk continues to rise for both models, with MODEL 1 showing a slightly larger increase than MODEL 2, aligning with future rainfall trends.

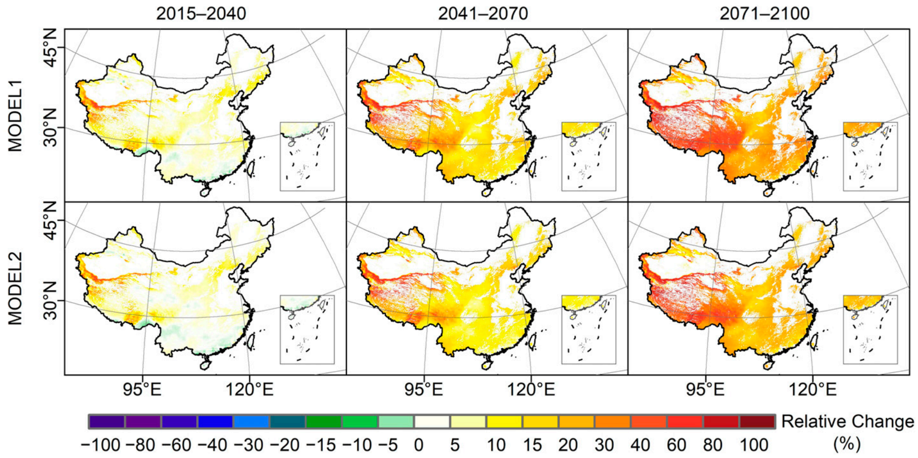

Figure 10. Spatial distribution of relative changes in rainfall-induced landslides in China under different landslide threshold models.

4.4.5. Spatiotemporal Changes in Landslide Risk Considering Multiple Factors

To visualize the spatiotemporal changes in rainfall-induced landslide risk in China under 180 different combinations, we calculated the mean, median, and 25th percentiles (Q1) and 75th percentiles (Q2). Figure 11 shows the relative changes in rainfall-induced landslide risk in medium- to high-sensitivity areas of China compared to the reference period across different future periods under climate change. The mean and median results are almost identical, indicating a general increase in landslide risk across most of China in the 21st century. In the early 21st century, most areas see an increase of less than 10%, with some regions, such as the Qinghai–Tibet Plateau and the Northwestern border areas, experiencing increases of over 20%. Conversely, some areas in the Southwest and Southeast show a decreasing trend, with reductions of less than 5%. By the mid-21st century, landslide risk in the Southwest and Southeast regions starts to increase by 10–15% compared to the historical period. The highest increase, about 40%, is still observed in the border areas of the Qinghai–Tibet Plateau and the Northwest, while the area of decline in the Qinghai–Tibet Plateau further reduces. By the late 21st century, increases in the Southeast, Northeast, and Southwest regions become more pronounced, with increases of over 20%. The 25th percentile shows a decreasing trend in landslide risk in China in the early 21st century, with decreases ranging from 5% to 15% compared to the reference period. By the mid to late 21st century, the trend shifts to an increase nationwide. The 75th percentile indicates increases of 5% to 30%, 15% to 60%, and over 30% in various regions compared to the reference period in the early, mid, and late 21st century, respectively.

Given the diverse and complex climate types in China, this study follows the method of Wang et al. [37] to facilitate the analysis of regional differences in landslides. The study area is divided into seven regions based on the similarity characteristics of China's regional climate. These regions are Northeast (NE), North (N), Southeast (SE), Southwest (SW), Eastern Northwest (ENW), Western Northwest (WNW), and Tibet.

Figure 12 illustrates the average changes in landslide risk relative to the reference period for each region across different seasons and time periods. Overall, landslide risk increases most significantly in spring and summer, with all regions generally seeing increases exceeding 10% during 2071–2100. The spring increases are particularly notable in the Southeast (SE), North (N), and Eastern Northwest (ENW) regions, reaching about 20%. Summer and autumn show relatively smaller increases, but still over 10% in most regions, with the highest summer increases in the Qinghai–Tibet Plateau (Tibet). Winter exhibits the smallest changes, with most regions having increases below 10%. In the early 21st century (2011–2040), the Southeast (SE) and Eastern Northwest (ENW) regions show a slight decreasing trend in landslide risk, generally less than 3%. However, over time, particularly in the late 21st century (2071–2100), landslide risk in these regions generally increases significantly.

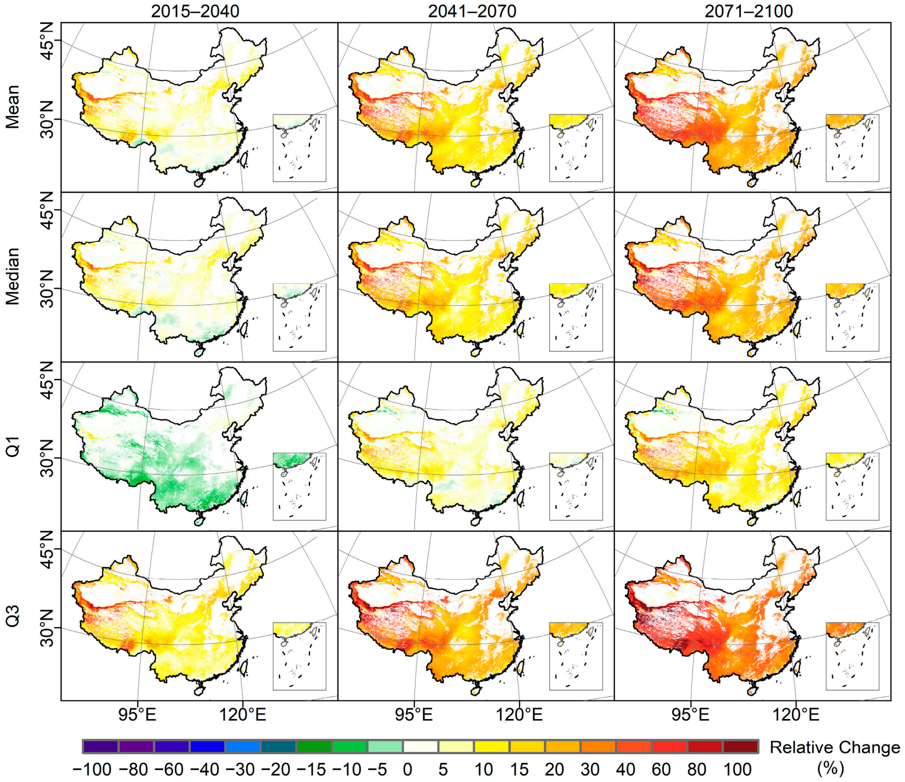

Figure 11. Spatial distribution of relative changes in rainfall-induced landslides in China across different future periods.

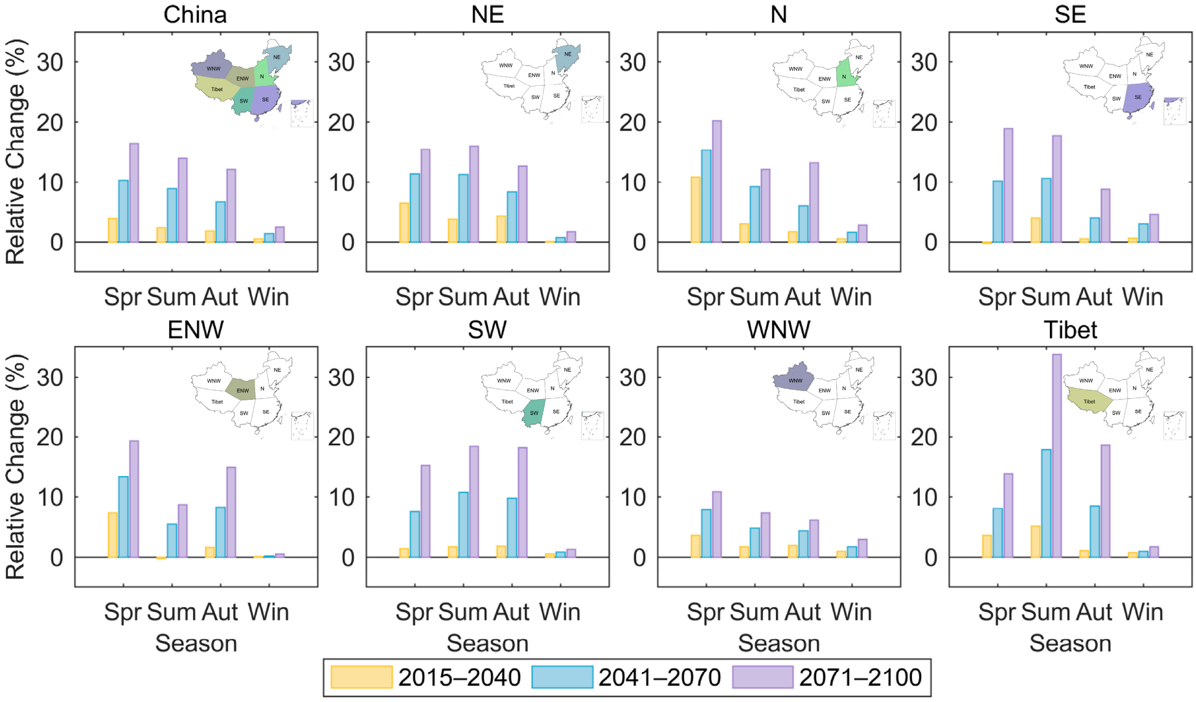

Figure 12. Seasonal changes in relative landslide risk across different periods for each region.

Although the landslide-risk prediction models developed in this study can predict the spatiotemporal distribution of rainfall-induced landslides in China under future climate change scenarios, several issues need to be addressed and improved. Many landslides in remote locations, especially in the Western regions, were not recorded in the landslide database used for constructing the threshold model, leading to an underestimation of rainfall-induced landslides. Additionally, some landslide records had ambiguous locations, dates, and triggering factors, affecting the accuracy and representativeness of the threshold model results.

5. Conclusions

This study conducted a prediction of rainfall-induced landslide risk in China using multi-scenario and multi-model climate data from CMIP6, with a focus on constructing rainfall-induced landslide threshold models and analyzing the spatiotemporal distribution of landslide risk.

Firstly, the study employed a fuzzy overlay model to integrate seven environmental disaster factors: slope, geological lithology, distance to fault zones, roads, water systems, urban expansion, and forest loss. This model calculates landslide sensitivity across China with a resolution of 1 km. Validation using historical landslide events shows that over 85% of these events fall within medium- to high- sensitivity areas. The sensitivity maps produced by this method effectively identify most landslide-prone areas and can be utilized in the development of subsequent landslide threshold models.

Additionally, different rainfall characterization methods were used to construct landslide threshold models. The threshold model based on the Antecedent Rainfall Index (ARI) showed higher accuracy and lower false alarm rates, proving more effective for landslide forecasting. Using this method, we derive 60 landslide thresholds from two landslide threshold models, two bias corrections, and 15 GCMs, which will be used for subsequent landslide risk prediction.

Finally, the study conducted the prediction of rainfall-induced landslide risk under multiple scenarios and models. In the early 21st century, the Qinghai–Tibet Plateau, Southwest, and parts of the Southeast regions showed a decrease in landslide risk by 5% to 10%, while other regions saw an increase of 5% to 20% compared to the reference period. By the mid-21st century, areas with decreasing risk continued to shrink, with most regions experiencing an increase of 10% to 40%. By the late 21st century, the nationwide risk had increased by more than 15%. Spatially, the increase in relative landslide risk showed a pattern of gradual increase from east to west.

Author Contributions: Conceptualization, Q.D.; data curation, H.Z. and J.Z.; formal analysis, H.Z. and J.Z.; methodology, H.Z.; software, J.Z. and H.Z.; writing—original draft, H.Z.; writing—review and editing, Q.D. and J.Z. All authors have read and agreed to the published version of the manuscript.

Funding: This research was funded by the National Natural Science Foundation of China (No. 42201020, No. 42371409) and the Natural Science Research of Jiangsu Higher Education Institutions of China (No. 22KJB170002).

Data Availability Statement: The original contributions presented in the study are included in the article, further inquiries can be directed to the corresponding author.

Conflicts of Interest: The authors declare no conflict of interest.

References

1. Liu, H.Z.; Xu, H.; Bao, H.J.; Xu, W.; Yan, X.F.; Xu, C.P. Characteristics analysis of rainfall-induced landslide thresholds in local regions. *J. Nat. Disasters* **2021**, *30*, 181–190.
2. Valenzuela, P.; Zêzere, J.L.; Domínguez-Cuesta, M.J.; García, M.A.M. Empirical rainfall thresholds for the triggering of landslides in Asturias (NW Spain). *Landslides* **2019**, *16*, 1285–1300. [CrossRef]
3. Liu, C.; Li, W.Y.; Wu, H.B.; Lu, P.; Sang, K.; Sun, W.W.; Chen, W.; Hong, Y.; Li, R.X. Susceptibility evaluation and mapping of China's landslides based on multi-source data. *Nat. Hazards* **2013**, *69*, 1477–1495. [CrossRef]
4. Lee, J.-U.; Cho, Y.-C.; Kim, M.; Jang, S.-J.; Lee, J.; Kim, S. The Effects of Different Geological Conditions on Landslide-Triggering Rainfall Conditions in South Korea. *Water* **2022**, *14*, 2051. [CrossRef]
5. Berhane, G.; Tadesse, K. Landslide susceptibility zonation mapping using statistical index and landslide susceptibility analysis methods: A case study from Gindeberet district, Oromia Regional State, Central Ethiopia. *J. Afr. Earth Sci.* **2021**, *180*, 13. [CrossRef]
6. Ermini, L.; Catani, F.; Casagli, N. Artificial Neural Networks applied to landslide susceptibility assessment. *Geomorphology* **2005**, *66*, 327–343. [CrossRef]

7. Segoni, S.; Lagomarsino, D.; Fanti, R.; Moretti, S.; Casagli, N. Integration of rainfall thresholds and susceptibility maps in the Emilia Romagna (Italy) regional-scale landslide warning system. *Landslides* **2015**, *12*, 773–785. [CrossRef]
8. Van Westen, C.J.; Rengers, N.; Soeters, R. Use of geomorphological information in indirect landslide susceptibility assessment. *Nat. Hazards* **2003**, *30*, 399–419. [CrossRef]
9. Shahabi, H.; Hashim, M. Landslide susceptibility mapping using GIS-based statistical models and Remote sensing data in tropical environment. *Sci. Rep.* **2015**, *5*, 9899. [CrossRef]
10. Abdı, A.; Bouamrane, A.; Karech, T.; Dahri, N.; Kaouachi, A. Landslide Susceptibility Mapping Using GIS-based Fuzzy Logic and the Analytical Hierarchical Processes Approach: A Case Study in Constantine (North-East Algeria). *Geotech. Geol. Eng.* **2021**, *39*, 5675–5691. [CrossRef]
11. Baum, R.L.; Savage, W.Z.; Godt, J.W. *TRIGRS—A Fortran Program for Transient Rainfall Infiltration and Grid-Based Regional Slope-Stability Analysis*, version 2; US Geological Survey Open File Report 2008-1159; U.S. Geological Survey: Reston, VA, USA, 2008.
12. Guzzetti, F.; Peruccacci, S.; Rossi, M.; Stark, C.P. Rainfall thresholds for the initiation of landslides in central and southern Europe. *Meteorol. Atmos. Phys.* **2007**, *98*, 239–267. [CrossRef]
13. Guzzetti, F.; Peruccacci, S.; Rossi, M.; Stark, C.P. The rainfall intensity-duration control of shallow landslides and debris flows: An update. *Landslides* **2008**, *5*, 3–17. [CrossRef]
14. Lee, K.T.; Ho, J.Y. Prediction of landslide occurrence based on slope-instability analysis and hydrological model simulation. *J. Hydrol.* **2009**, *375*, 489–497. [CrossRef]
15. Montgomery, D.R.; Dietrich, W.E. A physically based model for the topographic control on shallow landsliding. *Water Resour. Res.* **1994**, *30*, 1153–1171. [CrossRef]
16. Vaz, T.; Zêzere, J.L.; Pereira, S.; Oliveira, S.C.; Garcia, R.A.C.; Quaresma, I. Regional rainfall thresholds for landslide occurrence using a centenary database. *Nat. Hazards Earth Syst. Sci.* **2018**, *18*, 1037–1054. [CrossRef]
17. Caine, N. The Rainfall Intensity: Duration Control of Shallow Landslides and Debris Flows. *Geogr. Annaler. Ser. A Phys. Geogr.* **1980**, *62*, 23–27. [CrossRef]
18. Guzzetti, F.; Gariano, S.L.; Peruccacci, S.; Brunetti, M.T.; Marchesini, I.; Rossi, M.; Melillo, M. Geographical landslide early warning systems. *Earth-Sci. Rev.* **2020**, *200*, 102973. [CrossRef]
19. Jayakody, S.; Uzuoka, R.; Ueda, K.; Xu, J. Unsaturated slopes behavior under antecedent intermittent rainfall patterns: Centrifuge and numerical study. *Acta Geotech.* **2023**, *18*, 5773–5790. [CrossRef]
20. Kim, S.W.; Chun, K.W.; Kim, M.; Catani, F.; Choi, B.; Seo, J.I. Effect of antecedent rainfall conditions and their variations on shallow landslide-triggering rainfall thresholds in South Korea. *Landslides* **2021**, *18*, 569–582. [CrossRef]
21. Ma, T.; Li, C.; Lu, Z.; Wang, B. An effective antecedent precipitation model derived from the power-law relationship between landslide occurrence and rainfall level. *Geomorphology* **2014**, *216*, 187–192. [CrossRef]
22. Wicki, A.; Lehmann, P.; Hauck, C.; Seneviratne, S.I.; Waldner, P.; Stähli, M. Assessing the potential of soil moisture measurements for regional landslide early warning. *Landslides* **2020**, *17*, 1881–1896. [CrossRef]
23. Zhao, B.R.; Dai, Q.; Han, D.W.; Dai, H.C.; Mao, J.Q.; Zhuo, L.; Rong, G.W. Estimation of soil moisture using modified antecedent precipitation index with application in landslide predictions. *Landslides* **2019**, *16*, 2381–2393. [CrossRef]
24. Jemec Auflič, M.; Bezak, N.; Šegina, E.; Frantar, P.; Gariano, S.L.; Medved, A.; Peternel, T. Climate change increases the number of landslides at the juncture of the Alpine, Pannonian and Mediterranean regions. *Sci. Rep.* **2023**, *13*, 23085. [CrossRef]
25. He, S.; Wang, J.; Wang, H. Projection of Landslides in China during the 21st Century under the RCP8.5 Scenario. *J. Meteorol. Res.* **2019**, *33*, 138–148. [CrossRef]
26. Ge, S.; Wang, J.; Jiang, C. Projection of the precipitation-induced landslide risk in China by 2050. *Environ. Res. Lett.* **2024**, *19*, 024048. [CrossRef]
27. Jabbar, F.K.; Grote, K. Evaluation of the predictive reliability of a new watershed health assessment method using the SWAT model. *Environ. Monit. Assess.* **2020**, *192*, 224. [CrossRef]
28. Wu, J.; Gao, X.J. A gridded daily observation dataset over China region and comparison with the other datasets. *Chin. J. Geophys.* **2013**, *56*, 1102–1111.
29. Cannon, A. Multivariate quantile mapping bias correction: An N-dimensional probability density function transform for climate model simulations of multiple variables. *Clim. Dyn.* **2018**, *50*, 31–49. [CrossRef]
30. Cannon, A.; Sobie, S.; Murdock, T. Bias Correction of GCM Precipitation by Quantile Mapping: How Well Do Methods Preserve Changes in Quantiles and Extremes? *J. Clim.* **2015**, *28*, 6938–6959. [CrossRef]
31. Wood, A.W.; Maurer, E.P.; Kumar, A.; Lettenmaier, D.P. Long-range experimental hydrologic forecasting for the eastern United States. *J. Geophys. Res. Atmos.* **2002**, *107*, 4429. [CrossRef]
32. Xu, L.L.; Wang, A.H. Application of the Bias Correction and Spatial Downscaling Algorithm on the Temperature Extremes From CMIP5 Multimodel Ensembles in China. *Earth Space Sci.* **2019**, *6*, 2508–2524. [CrossRef]
33. Kirschbaum, D.; Stanley, T. Satellite-Based Assessment of Rainfall-Triggered Landslide Hazard for Situational Awareness. *Earth's Future* **2018**, *6*, 505–523. [CrossRef]
34. Stanley, T.; Kirschbaum, D.B. A heuristic approach to global landslide susceptibility mapping. *Nat. Hazards* **2017**, *87*, 145–164. [CrossRef]
35. Mirus, B.; Becker, R.; Baum, R.; Smith, J. Integrating real-time subsurface hydrologic monitoring with empirical rainfall thresholds to improve landslide early warning. *Landslides* **2018**, *15*, 1909–1919. [CrossRef]

36. Zhao, B.; Dai, Q.; Han, D.; Dai, H.; Mao, J.; Zhuo, L. Antecedent wetness and rainfall information in landslide threshold definition. *Hydrol. Earth Syst. Sci. Discuss.* **2019**, *2019*, 1–26. [CrossRef]
37. Wang, A.H.; Lettenmaier, D.P.; Sheffield, J. Soil Moisture Drought in China, 1950–2006. *J. Clim.* **2011**, *24*, 3257–3271. [CrossRef]